Welding in the World
https://doi.org/10.1007/s40194-024-01775-9

RESEARCH PAPER

Micro-macro modeling of tensile behavior of a friction stir welded hybrid joint of AlSi10Mg parts produced by powder bed fusion and casting

Aravindh Nammalvar Raja Rajan[1,2] · Marcel Krochmal[3] · Thomas Wegener[3] · Alexander Hartmaier[2] · Thomas Niendorf[3] · Ghazal Moeini[1]

Received: 22 August 2023 / Accepted: 8 April 2024

Abstract
Additive manufacturing (AM) has gained considerable interest due to its ability to produce lightweight parts with hierarchical microstructures. However, the current constraints on the build chamber size in powder-bed fusion type AM processes limit its industrial application. A hybrid welded joint, consisting of an AM-processed and a conventionally manufactured part, can be employed to produce larger components. Due to the varying processing conditions, these hybrid welded joints contain a wide range of microstructural heterogeneities, which influences the mechanical properties of the joint. Using a numerical model to predict the mechanical behavior of welded joints by considering the microstructural variations is essential for the safe and reliable implementation of hybrid welded joints. This study aims to predict the local tensile behavior of each region of a hybrid friction-stir welded joint of AlSi10Mg produced by laser-based powder bed fusion and casting using a microstructure-sensitive model as well as the global tensile behavior by considering the properties of each region using a joint macroscopic model. The results from this modeling approach agree well with the experimental results. Therefore, this method can predict the mechanical behavior of hybrid welded joints and can establish the structure–property relationship in each weld region.

Keywords Additive manufacturing · Friction stir welding · Casting · Crystal plasticity · Multiscale modeling · Aluminum–silicon alloy

1 Introduction

Additive manufacturing (AM) processes fabricate parts by depositing layer upon layer of material based on three-dimensional (3D) computer-aided design data. This facilitates AM to produce parts with intricate structures that are not achievable by conventional manufacturing processes. Among various AM processes, laser-based powder bed fusion of metals (PBF-LB/M) is the most widely used technique, especially for aluminum alloys, due to its ability to produce components with high geometrical accuracy. AlSi10Mg produced by PBF-LB/M is being widely investigated due to its lightweight characteristics and good mechanical properties. Nonetheless, the current limitation of the build chamber size restricts the usage of the PBF-LB/M process to produce only parts with relatively small dimensions. This part size constraint limits the application of PBF-LB/M AlSi10Mg parts in the automobile and aerospace industries. The part size limitation of the PBF-LB/M process can be overcome by employing a hybrid welded joint (HWJ) consisting of AM-processed and conventionally manufactured (e.g., cast, milled) parts [1, 2].

The weldability of the AM-processed components has been widely investigated [3–8]. Emmelmann et al. [3]

✉ Aravindh Nammalvar Raja Rajan
aravindh.rajan@w-hs.de

✉ Ghazal Moeini
Ghazal.Moeini@w-hs.de

[1] Institute of Mechanical Engineering, Westphalian University of Applied Sciences, Neidenburger Straße 43, 45897 Gelsenkirchen, Germany

[2] Interdisciplinary Centre for Advanced Materials Simulation (ICAMS), Ruhr University Bochum, Universitätsstr. 150, 44801 Bochum, Germany

[3] University of Kassel, Institute of Materials Engineering – Metallic Materials, Mönchebergstraße 3, 34125 Kassel, Germany

Published online: 29 April 2024

studied the effect of laser welding on PBF-LB/M processed AlSi12 alloy. The microstructural analysis revealed a high accumulation of pores in the weld zone (WZ). A similar accumulation was also observed when the electron beam welding was used to join PBF-LB/M AlSi10Mg workpieces. The solidification of the melt pool after the fusion weld processes led to a high percentage of porosity in the WZ. The porosity can be reduced by effectively controlling various welding processes, such as weld speed [3, 4]. To avoid the solidification-associated defects in the weld area, Hassanin et al. [5] investigated the applicability of solid state welding processes to join Ti6Al4V and AlSi10Mg specimens fabricated by the PBF-LB/M process. They concluded that friction stir welding (FSW) can produce defect-free welded joints. Prashanth et al. [6] tested the mechanical properties of the friction stir welded PBF-LB/M AlSi12. The results showed a degradation of the hardness in the WZ and heat-affected zones (HAZ). The tensile strength of the welded joint was also inferior to the PBF-LB/M AlSi12. However, the ductility of the welded specimens was considerably higher than that of the AM-processed specimens. Previous studies by some of the present authors [7–9] on the friction stir welded/processed PBF-LB/M Al parts also concluded the degradation in the hardness and tensile strength and inferior low-cycle fatigue properties at higher strain amplitude. These variations in the mechanical properties can be attributed to the change in the morphology of the Si-rich phase due to severe plastic deformation [6–9]. Recently, some of the authors of the present study [1] examined the microstructure and mechanical properties of the hybrid FSW joint of AlSi10Mg produced by PBF-LB/M and casting. The properties of the PBF-LB/M-cast joint were significantly inferior to the PBF-LB/M-PBF-LB/M joint but more or less similar to the cast-cast joint. The cast part was found to be the reason for such a drastic decrease in the properties of the hybrid joint, and the crack initiation always occurred in the cast region. Despite the availability of experimental investigation, there is still a lack in the numerical aspect of the HWJ.

The crystal plasticity (CP) model has been extensively used to determine the mechanical behavior of PBF-LB/M AlSi10Mg [10–13]. The authors of the present study [12, 13] applied a microstructure-sensitive hybrid CP-J2 model to the dual-phase representative volume elements (RVE) to predict the tensile and fatigue behavior of the PBF-LB/M AlSi10Mg and its heat-treated counterparts. The validation with the experimental results showed that the applied modeling framework can accurately predict the mechanical behavior of the PBF-LB/M alloys. For the welded joints, Toursangsaraki et al. [14] used a micro-macro modeling approach to determine the tensile properties of an AA2195-T6 FSW joint by considering the microstructural aspects of each joint region. To predict the properties of each weld area, they created the synthetic RVEs from the experimentally observed microstructure. In addition, they have enriched the CP model to consider the effect of precipitate hardening that occurs in the material. The tensile behavior of each region predicted by the CP model agreed well with results obtained using the digital image correlation (DIC) method. Afterward, they used the predicted stress–strain curve of each joint region to estimate the global tensile behavior of the welded joint. The macrojoint model that considered the behavior of each region predicted the global stress–strain curve as well as the failure location accurately. Therefore, this method can be employed to predict the tensile behavior of AM-cast hybrid FSW joint and to establish the structure–property relationship for each joint region.

The wide range of microstructural variations observed in an HWJ affects its structural integrity. Therefore, the effect of the microstructural features of each region on its mechanical properties must be established to implement the hybrid joint in industrial applications. A microstructure-based numerical modeling approach is an efficient way to achieve it. This study aims to predict the tensile behavior of each joint region (AM, cast, WZ, and HAZ) using a hybrid CP and J2-plasticity formulation and of the entire AM-cast FSW joint using the result from micromechanical modeling. The results from the micromechanical modeling approach and the joint macro model are compared with the experimental results to assess the accuracy of the applied modeling approaches.

2 Specimen fabrication and microstructural characterization

For the present study, sheet material (150 mm×40 mm×5 mm) was fabricated using the gravity die-casting and PBF-LB/M processes. For PBF-LB/M, a SLM 280^{HL} (SLM Solutions, Lübeck, Germany) machine and commercially available AlSi10Mg powder material were used. The parameter set for manufacturing of the specimens included a scanning speed of 1170 mm/s, a laser power of 400 W, a layer thickness of 60 µm, and a hatch spacing of 0.2 mm. Moreover, argon was used as a shielding gas during manufacturing. For a more detailed description of the manufacturing process, the reader is referred to a previous study of the authors [1]. The sheets were then welded together in a butt-joint configuration with the AM sheet on the advancing side (AS). This was done using the FSW process on a PTG heavy industries FSW machine (cf. Fig. 1a) with the process parameters shown in Table 1. An offset of 1 mm towards the as-cast material was applied to encourage a high density in the welded area, while the AM portion of the joint was still plasticized 1.5 mm into the nugget area. The welding experiments were conducted using suitable clamping and fixing devices. All specimens were

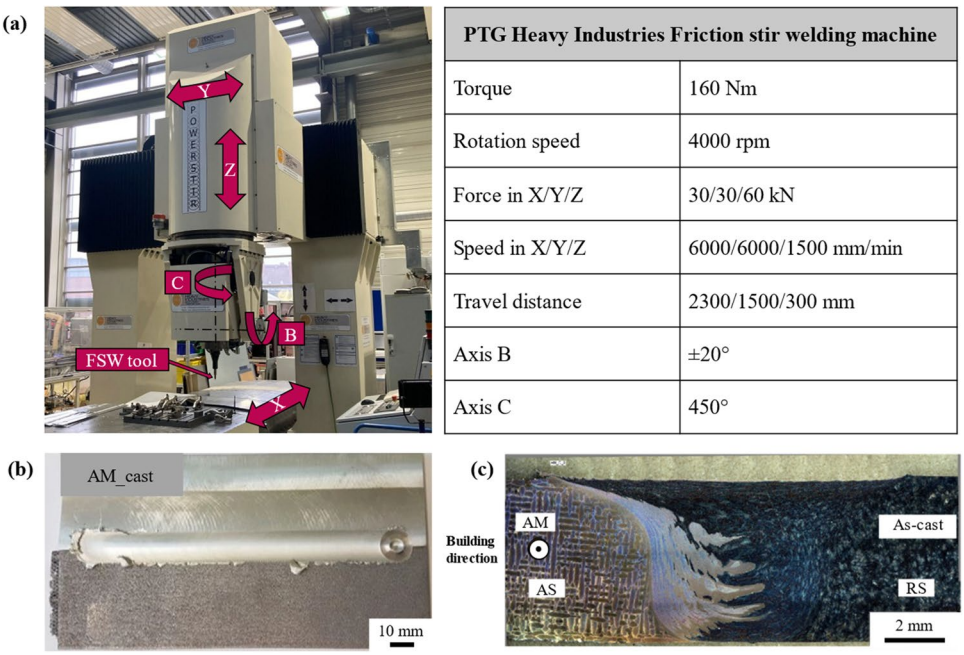

Fig. 1 **a** Technical specifications of the used FSW machine, **b** macroscopic overview of the weld seam, reproduced from Ref. [15], and **c** etched cross-section of the weld area, recompiled from Ref. [1]

Table 1 Process parameters used for FSW experiments

Process parameters	Values
Tool rotation speed	800 rpm
Tool travel speed	400 mm/min
Pin length	5–5.1 mm
Tool pin geometry	Metric M5 thread
Tool shoulder diameter	12 mm
Tool pin material	X40CrMoV5-1
Tool inclined angle	2°
Control type	Position-controlled
Position offset towards cast sheet	1 mm

tested in the condition directly resulting from the process considered, meaning no post-process heat treatments were considered. No welding preparation was carried out either; i.e., the sheets were welded in as-built (PBF-LB/M) and machined (cast) surface conditions. As can be seen in Fig. 1, FSW with the aforementioned parameter set resulted in sound welds without apparent inside or outside welding defects. For a comprehensive analysis of the resulting microstructural and mechanical features, the reader is referred to a previous publication [1], which serves as the basis for the present study.

For tensile testing, a screw-driven MTS criterion testing system was employed. Testing was conducted in displacement control using a constant crosshead speed of 2 mm/min. An MTS miniature extensometer, featuring a gauge length of 5 mm, was used for strain measurements. For all tensile tests conducted within this study (of each welded region), miniature specimens with a gauge section of 8 mm × 3 mm × 1.6 mm (1 mm for HAZ specimens) were cut parallel to the welding direction using electrical discharge machining. All surfaces of the specimens were ground using silicon carbide grinding paper up to a grit size of P1200. For HWJ, the results obtained from tensile tests in Ref. [1] were used in this study.

For microstructural characterization of the hybrid joint, secondary electron (SE) and electron backscatter diffraction (EBSD) investigations were carried out using a Zeiss ULTRA GEMINI (Oberkochen, Germany) high-resolution scanning electron microscope (SEM). The analysis of SEM and EBSD data revealed a wide range of microstructural heterogeneities along the length of the HWJ, as shown in Fig. 2. The AM region is characterized by coarse columnar and some equiaxed grains, with a continuous network-patterned Si-rich phase around the Al cells inside each grain [7, 16]. In contrast, the cast region has much larger grains with a size of approximately 1 mm and a long elliptical secondary phase dispersed in it. The size of the elliptical Si-rich phase is similar to that of the large columnar grains observed in the AM microstructure. Due to severe plastic deformation during FSW, grain refinement occurs in the WZ. In addition, the Si-rich network in the AM region and the Si-rich elliptical particles are broken to form equiaxed particles [1]. The HAZ shows the characteristics of both the base material and WZ. Since the thermo-mechanically affected zones are extremely small, they could not be characterized separately. These microstructural variations lead to a heterogenous mechanical behavior along the joint, as evident from the microhardness map shown in Fig. 2. Therefore, each region's microstructural characteristics

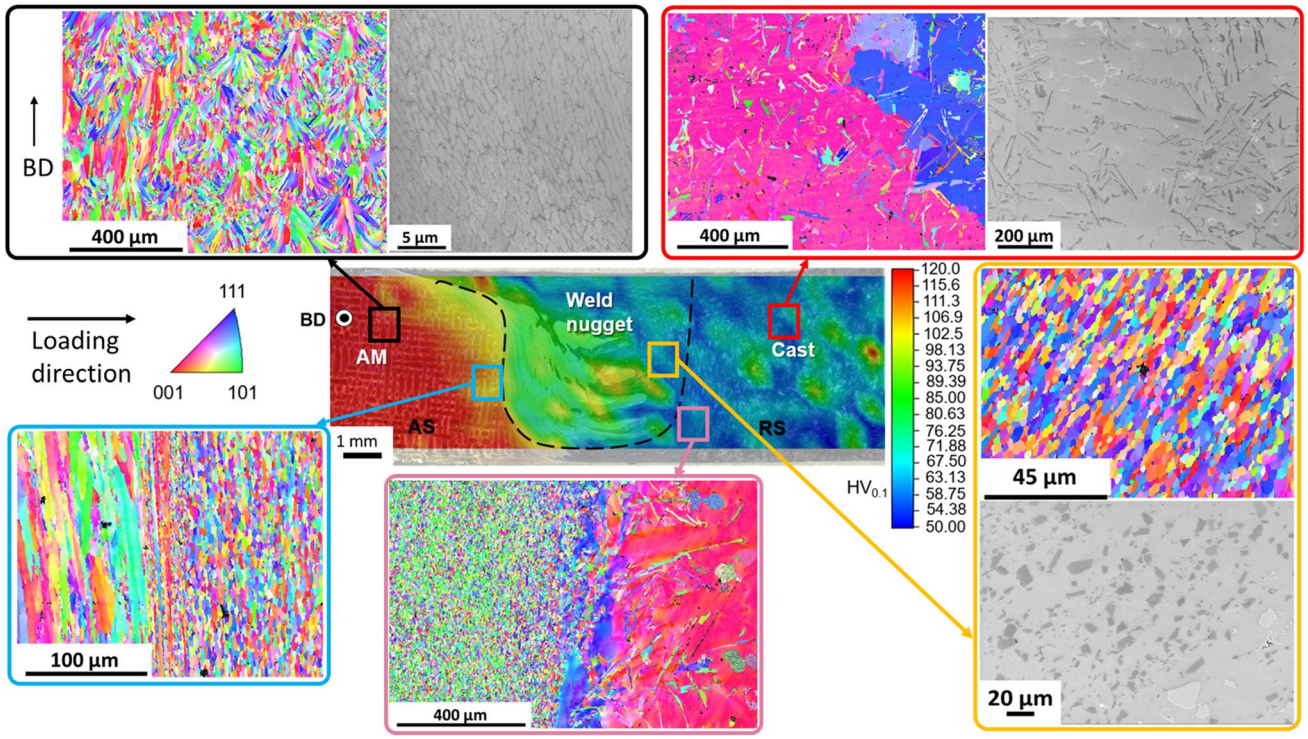

Fig. 2 Microstructure and microhardness map of the friction-stir welded hybrid joint. The EBSD inverse pole figures are plotted along the loading direction (AS - advancing side; RS - retreating side; and BD - build direction). Except for the EBSD map of the HAZ on the AM side, all the images have been reproduced from previous studies of the authors [1, 12]

must be considered to predict the mechanical behavior of the AM-cast HWJ.

3 Micro-macro modeling of AM-cast hybrid welded joint

Since a large variation in microstructure is observed along the length of the HWJ, the effect of microstructural characteristics of each joint region must be investigated in-depth, to understand and predict the mechanical properties of the entire joint. Thus, to accurately predict the tensile behavior of the HWJ, a micro-macro modeling approach must be used. Figure 3 shows the schematic diagram of the applied modeling approach. A suitable material model that considers the material's microstructure to describe its mechanical behavior and an RVE that mimics the experimentally observed microstructure are required to predict the tensile behavior of each region in the micro scale. Then, a scale-bridging technique has to be employed to convert the result from microscale to macroscale results. The stress–strain curves of each region obtained from the micromechanical model must be applied to each region in the joint macro model to predict the HWJ's tensile properties. The following sections will explain in detail all the aspects considered in the present study.

3.1 Constitutive modeling framework and scale-bridging

The present study uses a hybrid constitutive model [12, 13] to describe the tensile behavior of each joint region. It consists of a CP model for the Al phase and a J2-plasticity model for the Si-rich phase.

A rate-independent phenomenological CP model is used to describe the behavior of the Al phase. A brief overview of the CP model is given here. For a detailed description of the model, the reader is referred to previous studies [17–19].

The total deformation ($F=F_eF_p$) is obtained from the reversible lattice deformation (F_e) and irreversible lattice deformation (F_p). Since plastic deformation in a polycrystalline material is caused by dislocation movement along activated slip systems, the plastic velocity gradient is defined as the sum of all slip rates along all the slip systems.

$$\boldsymbol{L}_p = \dot{\boldsymbol{F}}_p \boldsymbol{F}_p^{-1} = \sum_{\alpha=1}^{N_s} \dot{\gamma}^{\alpha} \tilde{\boldsymbol{M}}^{\alpha}, \tag{1}$$

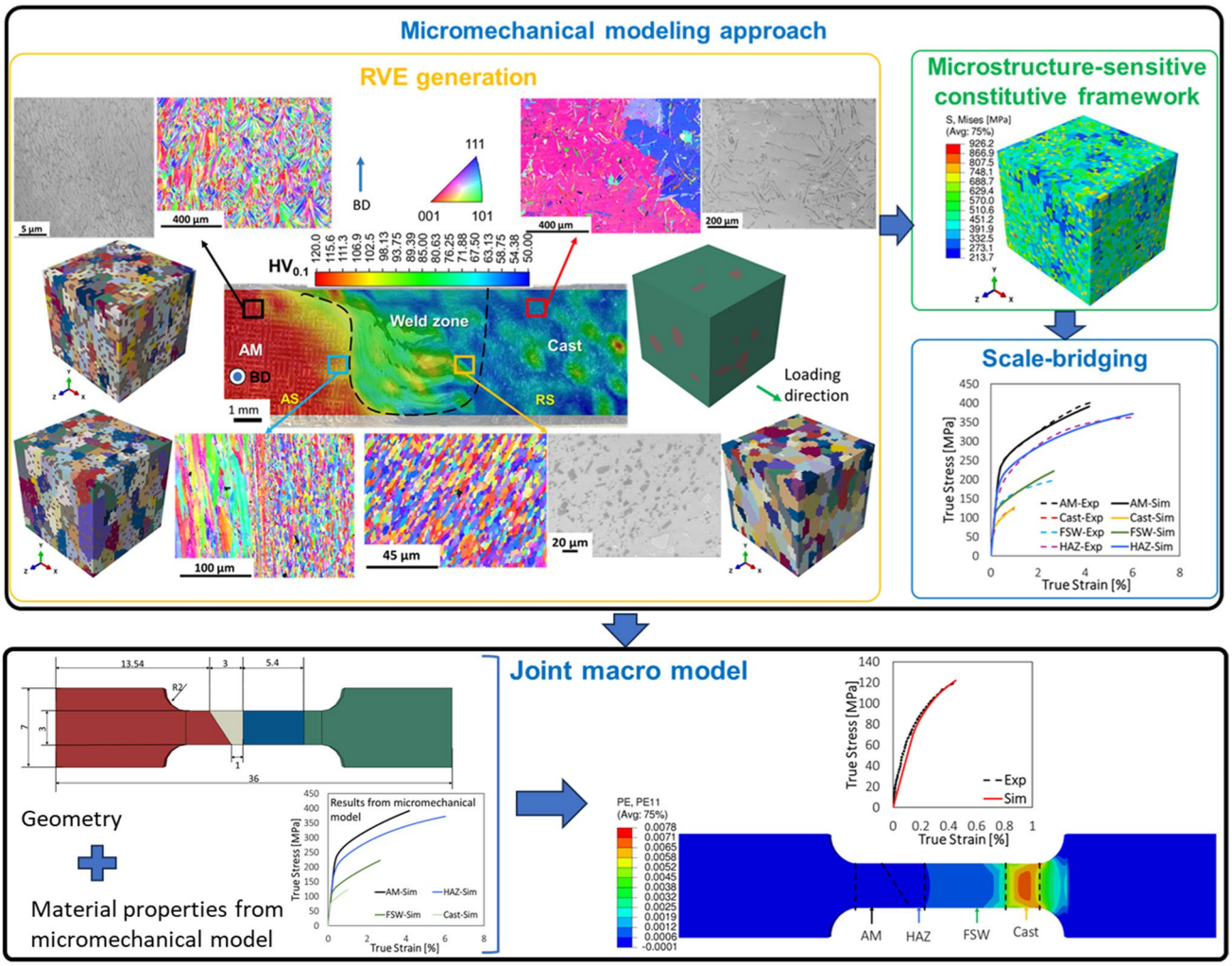

Fig. 3 Schematic diagram of the micro–macro modeling approach used in the present study

where $\dot{\gamma}^{\alpha}$ is the shear rate of the slip system α, N_s denotes the number of slip systems, and $\widetilde{\boldsymbol{M}}^{\boldsymbol{\alpha}}$ denotes the Schmid tensor. The Schmid tensor is the dyadic product of the slip direction ($\boldsymbol{d}^{\alpha}$) and the slip plane normal ($\boldsymbol{n}^{\alpha}$).

$$\widetilde{\boldsymbol{M}}^{\boldsymbol{\alpha}} = \boldsymbol{d}^{\alpha} \otimes \boldsymbol{n}^{\alpha}. \tag{2}$$

The resolved shear stress (τ^{α}), which denotes the internal stress state, is approximated using the elastic strain on each slip system.

$$\tau^{\alpha} = \frac{\widetilde{\mathbb{C}}}{2}\left(\boldsymbol{F}_e^{\boldsymbol{T}}\boldsymbol{F}_e - \boldsymbol{I}\right) : \widetilde{\boldsymbol{M}}^{\boldsymbol{\alpha}}. \tag{3}$$

Here, $\widetilde{\mathbb{C}}$ and $\boldsymbol{I}$ denotes the fourth-order elasticity tensor and the second-order identity tensor, respectively. The shear rate can be formulated as a function of resolved shear stress (τ^{α}) and slip resistance ($\widehat{\tau}^{\alpha}$):

$$\dot{\gamma}^{\alpha} = \dot{\gamma}_0 \left| \frac{\tau^{\alpha}}{\widehat{\tau}^{\alpha}} \right|^{p_1} sgn(\tau^{\alpha}), \tag{4}$$

where $\dot{\gamma}_0$ is the reference shear rate and p_1 denotes the inverse of the strain rate sensitivity. The evolution of the slip resistance can be described by considering the influence of any slip system (β) on a fixed slip system (α) using isotropic hardening as follows:

$$\dot{\widehat{\tau}}_c^{\alpha} = \sum_{\beta=1}^{N_s} h_0 q_{\alpha\beta} \left(1 - \frac{\widehat{\tau}^{\beta}}{\widehat{\tau}^{f}}\right)^{p_2} \left|\dot{\gamma}^{\beta}\right|. \tag{5}$$

Here, $q_{\alpha\beta}$ is the cross-hardening matrix, h_0 is the hardening rate, p_2 is a fitting parameter, and $\widehat{\tau}^{f}$ denotes the saturation slip resistance related to the dislocation accumulation. The diagonal and off-diagonal elements in the cross-hardening matrix represent the coplanar and noncoplanar slip

systems, respectively. The diagonal and off-diagonal elements are set as 1.0 and 1.4, respectively. The CP model is implemented in ABAQUS [20] using a user-material subroutine (UMAT).

For the Si-rich phase, a J2-plasticity model is used. According to von Mises yield criteria, when the second invariant of the deviatoric stress tensor reaches a critical value associated with the yield strength, plastic yielding starts [21]. Thus, the von Mises function (ϕ) can be represented as [22]:

$$\phi = \sqrt{\frac{3}{2}\tilde{\sigma}^D : \tilde{\sigma}^D} - Y\left(\bar{\varepsilon}_p\right), \tag{6}$$

where $\tilde{\sigma}^D$ is the deviatoric part of the stress tensor and $Y\left(\bar{\varepsilon}_p\right)$ denotes the yield strength as a function of plastic strain. An associative flow rule where the plastic strain increment is proportional to the gradient of yield surface is used.

The Voce law depicts the isotropic hardening behavior of the Si-rich phase. The Voce law is represented as [12, 13]:

$$Y\left(\bar{\varepsilon}_p\right) = \sigma_y + K\left(1 - e^{-n\bar{\varepsilon}_p}\right), \tag{7}$$

where σ_y is the initial yield stress and K and n denote the saturation stress and the Voce law exponent, respectively. For the J2-plasticity model, the standard model available in ABAQUS [20] is used.

3.1.1 Parameterization of the CP and J2-plasticity models

The material behavior of the Al and Si-rich phases must be characterized separately to calibrate the unknown parameters of the CP and J2-plasticity models. Thus, the nanoindentation tests are performed on the Al and Si-rich phases in each region using a Berkovich indenter. Multiple indentations are performed to account for scatter in the nanoindentation results due to the influence of one phase on another. The HAZ on the cast side is neglected since there is no difference in the hardness value between weld and cast zones (cf. Fig. 2). Since the effect of the very-fine Si precipitates in the WZ cannot be resolved in nanoindentation tests, the WZ RVE does not consider the Si-rich phase. Based on the analysis of the nanoindentation test results, the Si phase in the cast region is considered as elastic material.

In the CP model, the reference shear rate ($\dot{\gamma}_0$) and the fitting parameter (p_2) are 0.001 1/s and 2.5, respectively. The three elastic constants of the Al phase are $C_{11} = 107.3$ GPa, $C_{12} = 60.9$ GPa, and $C_{44} = 23.8$ GPa [10]. The remaining four CP model parameters ($p_1, \hat{\tau}_0^{\alpha}, h_0, \hat{\tau}^f$) must be calibrated. Young's modulus and Poisson's ratio for the Si-rich phase are 66,700 MPa [10] and 0.33 [17], respectively. Three remaining parameters (σ_y, K, and n) are unknown and must be calibrated.

To extract the unique parameters, the inverse analysis procedure uses both the surface profile and force–displacement curves. The trust-region reflective algorithm [23], available in the open-source Python library SciPy [24], solves the inverse analysis problem. The normalized root mean squared error (cf. Equation 8), which considers the error of the force–displacement and surface profile curves, is taken as an objective function.

$$NMRSE = \frac{1}{max\left(f_{FD}^{exp}\right)}\sqrt{\frac{1}{r}\sum_{n=1}^{r}\left(f_{FD}^{exp} - f_{FD}^{sim}\right)^2} + \frac{1}{min(D_{ST}^{exp})}\sqrt{\frac{1}{q}\sum_{i=1}^{q}\left(D_{ST}^{exp} - D_{ST}^{sim}\right)^2} \tag{8}$$

where subscripts *FD* and *ST* represent force–displacement and surface topology curves, respectively, and superscripts exp and sim denote the experiment and simulation, respectively. f and D illustrate the force and the displacement value. The calibrated values are given in Table 2, and the fitted curves are shown in Fig. 4.

3.1.2 Scale-bridging

A first-order computational homogenization technique is used for scale-bridging. In this scheme, the macroscopic stress and strains are obtained by volume averaging the microscopic quantities [25]. The general form of first-order homogenization is given as follows:

Table 2 Calibrated parameters of the CP and J2-plasticity models of different weld regions. The parameters of AM region was calibrated in the previous study of the authors [12]. For detailed description of inverse analysis procedure refer the text in Section 3.1.1

Weld regions	CP model parameters				Voce law parameters		
	p_1[−]	$\hat{\tau}_0^{\alpha}$[MPa]	$\hat{\tau}^f$[MPa]	h_0 [MPa]	σ_y[MPa]	K [MPa]	n [−]
AM [12]	52	93	190	1117	271.38	803	20
HAZ	66	75	197	1121	302.5	445.78	64.05
Cast	80	35	155	898	-	-	-
WZ	76	48	229	1143	-	-	-

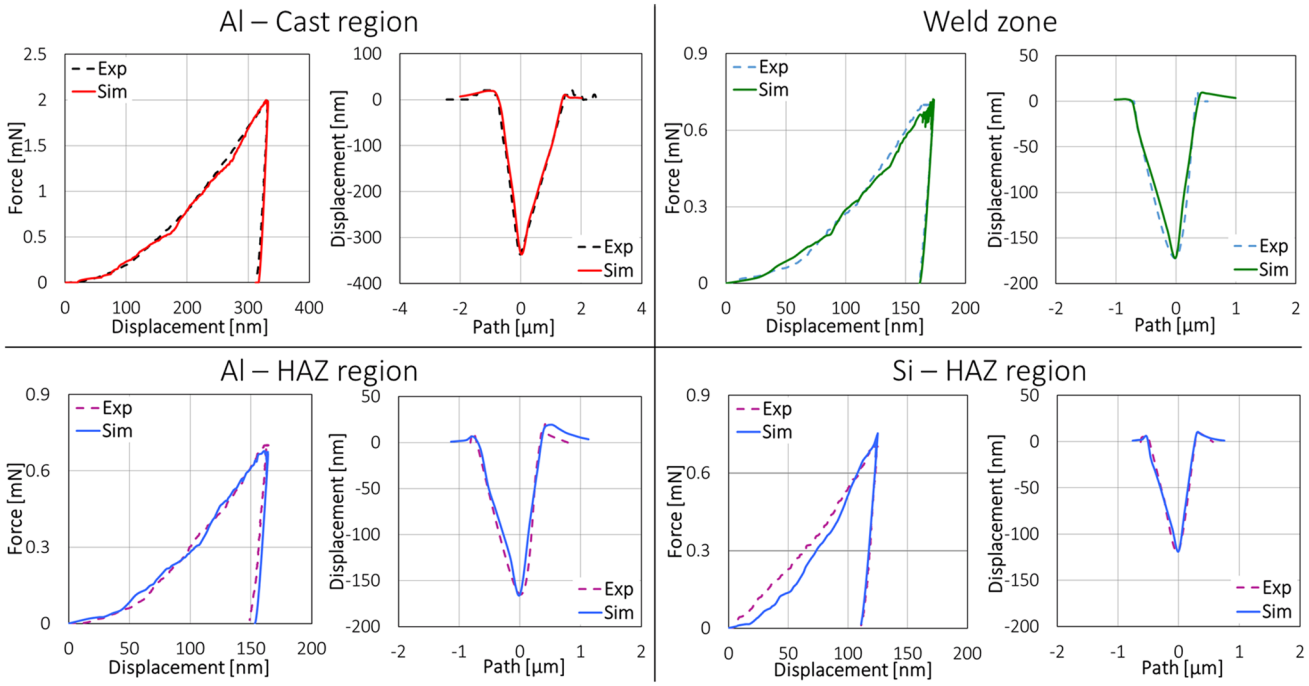

Fig. 4 Comparison of the force–displacement and the surface profile curves obtained from experimental test and numerical model using the calibrated parameters. See text for details regarding the calibration method and refer Table 2 for calibrated parameters. For AM results, the reader is referred to the previous publication [12]

$$\bar{\xi} = \frac{1}{V_{SM}} \int_{V_{SM}-} \xi dv. \tag{9}$$

Here, ξ and $\bar{\xi}$ denote the microscopic and macroscopic quantities, respectively, and V_{SM} is the volume of the synthetic microstructure.

3.2 Generation of the joint macromodel and the synthetic microstructure of each region

For macroscopic modeling, a 3D joint macromodel is created in ABAQUS and meshed using C3D8 elements. Each zone is separated based on the dimensions observed in the experimental tensile specimen, as shown in Fig. 5 a and b. The tensile properties from the RVE of each region are assumed to be homogeneously distributed in that region on the macromodel.

An understanding of the heterogeneous microstructure and the evolution of the local stress–strain is required to investigate the mechanical behavior of the FSW joint [14]. Therefore, a statistically equivalent RVE must be created for each weld region, and the CP model must be applied to study the behavior at the grain scale. The RVEs of AM, HAZ, and WZ (cf. Fig. 5 c–e) regions are created using Kanapy [26]. Since the RVE size does not influence the prediction of the tensile properties [12], the RVEs of AM, HAZ, and WZ are created such that each RVE has a minimum of 500 grains and has a minimum number of elements to reduce computational time. The statistical inputs required by Kanapy are extracted using MTEX [27] from the EBSD maps shown in Fig. 2. Using these inputs, the Kanapy creates the RVE with the required grain morphology and then assigns the representative orientations to the RVE grains using an orientation assignment algorithm [28] based on the surface area. Figure 5 c–e also compare the RVE data with the experimentally observed EBSD data. It can be seen that the orientation distribution function plot of the RVE and EBSD maps agree well with each other. The plots of the equivalent diameter and aspect ratio reveal that the probability densities of RVEs are higher than that of the EBSD data. This is due to the maximum and minimum cut-off values used during the RVE generation. However, the plot shows that the RVE captures the grain morphologies that are predominantly observed in the EBSD maps. After creating the RVEs, the Si-rich phase is randomly distributed in the RVEs based on the volume fraction in SE of each region (except WZ RVE) using Python code. For a detailed description of the RVE generation using Kanapy, the reader is referred to the previous publications of the authors [12, 13]. For the cast region, a single-grain RVE with elongated Si-rich particles is created using DREAM.3D [29] (cf. Fig. 5 f) using the statistical information of both the Al and Si-rich phases from the experimental EBSD map shown in Fig. 2. The orientation of the largest grain

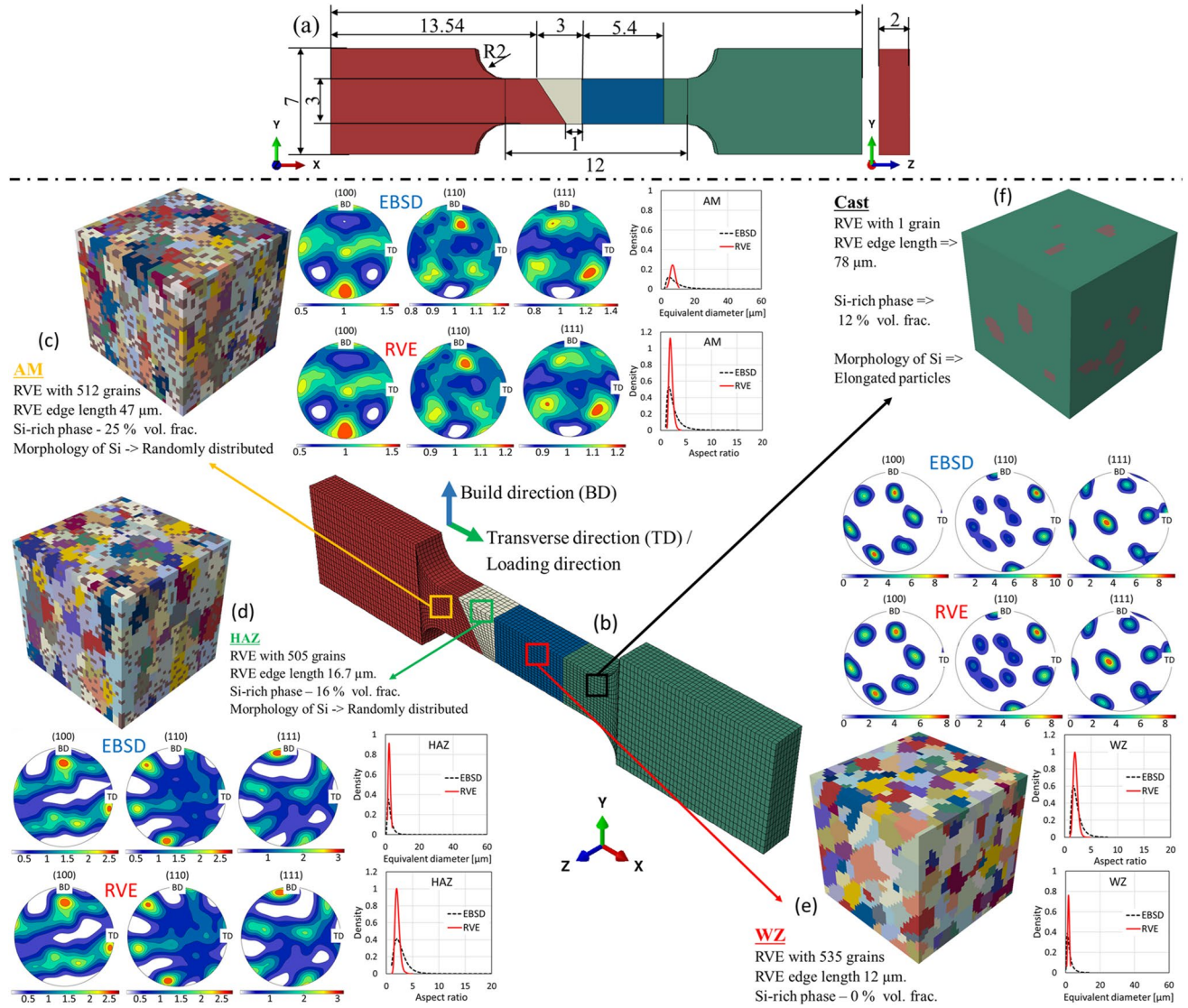

Fig. 5 The joint macro model and the RVE of each weld region with the statistical comparison of the RVE data with the experimentally observed EBSD data. **a** and **b** Macromodel of a hybrid FSW joint with various regions separated based on their dimensions. **c**, **d**, and **f** Dual-phase RVEs of AM, HAZ, and cast regions, respectively (Si-rich phase is represented in brown). **e** Single-phase RVE of the WZ without the Si-rich phase

is then extracted from the EBSD map and assigned to the RVE grain. A periodic boundary condition is applied to each RVE [19]. The RVEs and the macromodel are loaded along the transverse direction (*X*-direction).

4 Results and discussions

4.1 Prediction of the local tensile properties using hybrid micromechanical model

The local tensile properties of each weld region are predicted using the RVE, shown in Fig. 5, and the calibrated parameters of the respective joint area (cf. Table 2). Figure 6 compares the result from the micromechanical modeling approach (solid lines) of each weld region with the experimental tensile test results (dashed lines). It can be clearly seen that the result from the applied hybrid constitutive framework predicts the tensile behavior of the AM, HAZ, and cast regions with reasonably good accuracy. On the other hand, Fig. 6 shows a significant difference in the hardening rate between the simulation and the experimental curves in the WZ. A large variation is also observed in the experimental tensile tests of the WZ. These are attributed to the varying hardness inside the WZ (cf. Fig. 2). Therefore, the tensile results of the WZ are dependent on the region of

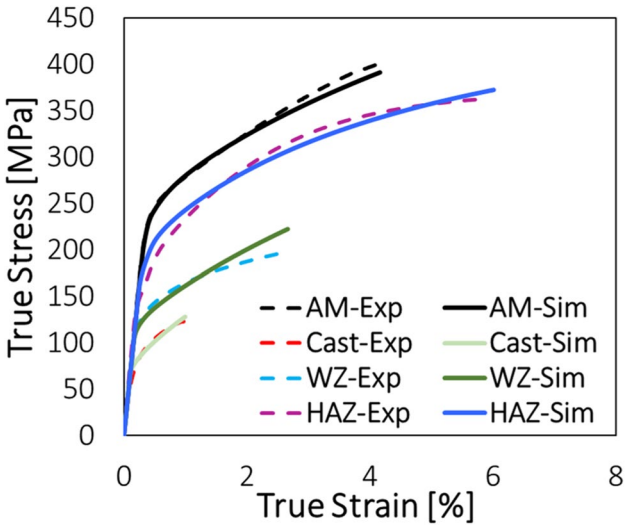

Fig. 6 Comparison of results from the micromechanical modeling approach with that from the tensile test of each weld region. The AM results are reproduced from the previous publication of the authors [12]

specimen extraction. Similarly, the nanoindentation results, used for parameter calibration, are also location dependent. In this study, multiple nanoindentation tests were performed on a localized region in the WZ. These nanoindentations could have been performed on the high hardness region, which would have influenced the plasticity parameters of the CP model. On the other hand, the tensile specimens extracted from the WZ contain both the high and low hardness regions. The difference between the predicted and the experimental results could be reduced by using nanoindentation curves obtained from the wider FSW region for the parameter extraction. Irrespective of that, the result of the WZ from micromechanical modeling is used as an input for the macro modeling approach since the total strain applied to the macro model is less than 2%, till which the deviation of experiment and simulation results of the WZ region is negligible.

The tensile behavior varies widely along the length of the HWJ, as illustrated in Fig. 6. A vast difference can be observed in the tensile properties of the two base materials. The cast region has the lowest strength among the different weld regions. The yield and ultimate strength of the cast region are approximately 60 MPa and 123 MPa, respectively, and the elongation to failure (EF) is about 1%. On the other hand, the AM region has the yield and ultimate strength of 220 MPa and 400 MPa, respectively, and an EF of 4.2%. The difference in tensile behavior between the PBF-LB/M and the cast AlSi10Mg is due to the shape and morphology of the Si particles, which is known to significantly affect the mechanical behavior of Al-Si alloys [30]. Due to the slow cooling rate during casting, the Si phase is precipitated to long elliptical or acircular particles distributed randomly in the Al grains, as shown in Fig. 2. In contrast, the PBF-LB/M process is characterized by multiple reheating cycles and rapid solidification. This leads to a unique network morphology of the Si-rich phase, which contains both eutectic Si and eutectic Al [16], around Al cells (cf. Fig. 2), and fine Si precipitates dispersed throughout the Al cells. Due to rapid solidification, the solid solution strengthening in AM AlSi10Mg occurs because of the difference in the atomic radii of Si and Al, creating a strain field, which in turn hinders the dislocation motion [31]. Along with the solid solution strengthening, the hindrance to the dislocation movement by the Si-rich phase at cell boundaries and Si fine precipitates due to Hall–Petch and Orowan looping mechanisms, respectively, provide much higher strength to AM AlSi10Mg than its cast counterpart [31]. The effect of the solid solution strengthening and the Orowan looping mechanism due to the Si fine precipitates dispersed in the Al cells can be seen in the evolution of the stress–strain of the Al phase, as illustrated in Fig. 7 a. These strengthening mechanisms are not modeled in the CP model. Instead, these behaviors are captured during the nanoindentation tests of the Al phase in each weld region, which in turn is reflected in the stress–strain curves through calibrated CP parameters. Due to the above-mentioned strengthening mechanisms, the strength of the Al phase in the AM region is much higher than that in the cast region. In the cast region, due to the lower strength of the Al phase, a homogeneous stress distribution occurs in the Al phase, as evident from Fig. 7 c. On the other hand, much higher stress is accumulated in the Si particles (cf. Fig. 7 g). This could act as a crack initiation region. Seifeddine et al. [32] showed that failure of a cast Al alloy is caused by brittle fracture of the needle-shaped intermetallic secondary phase. In contrast, in the AM RVE, an inhomogeneous distribution is seen in the Al phase due to the grain orientations (cf. Fig. 7 b), and high stresses are distributed in the Si-rich phase (cf. Fig. 7 f).

Severe plastic deformation during the FSW process breaks the Si-rich network and particles, producing globular Si-rich particles and very fine Si precipitates dispersed in the Al phase. This morphology provides better tensile properties than the cast specimen. However, the removal of the solid solution strengthening and the Si-rich network associated Hall–Petch effect leads to an inferior tensile behavior compared to the AM region. The change of Si morphology from network to globular form has been found to improve ductility at the expense of strength [12, 33]. However, it can be seen from Fig. 6 that the ductility of the FSW zone is less than the AM part. This can be attributed to the characteristics of the cast specimen found in the weld zone, as evident from lower hardness at the top right corner of the weld zone (cf. Fig. 2). Basically, as both the AM and the cast region experience grain and particle refinement during welding, the weld zone

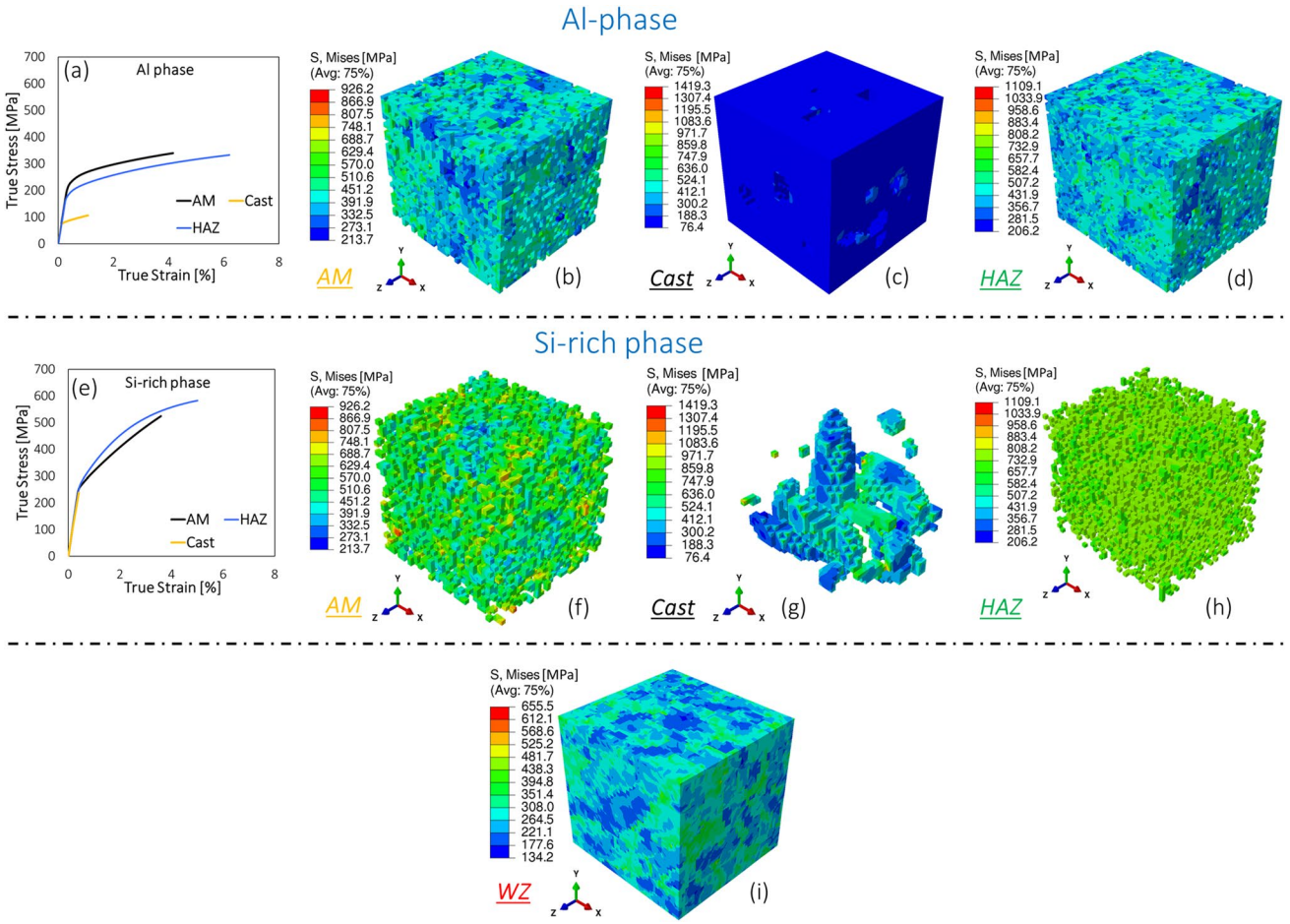

Fig. 7 Phase stress–strain curves and von Mises equivalent stress distribution of each weld region at their maximum applied strain. **a** Stress–strain curves of the Al phase of AM, HAZ, and the cast regions. **b** to **d** von Mises stress distribution in the Al phase of AM, cast, and HAZ, respectively, at their respective maximum applied strain. **e** Phase stress–strain curves of the Si-rich phase of three welded regions. **f** to **h** Von Mises stress distribution in the Si-rich phase of the two base regions and the HAZ of the Hybrid FSW joint. **i** Von Mises equivalent stress distribution if the weld zone at the applied strain of 2.7%

that was originally an AM part still has a much finer particle distribution than the weld zone that was initially a cast part. Tensile specimens extracted from the weld zone, featuring material from both sides, are, therefore, still affected by the initial cast state, which is assumed to be the reason for the reduced EF compared to the AM specimens. Figure 7 i shows a heterogeneous stress distribution due to the grain morphology and orientation observed in the WZ RVE.

The thermal load in the HAZ region during the FSW process causes the Si-rich cell structure to disintegrate and weaken the solid solution strengthening obtained during the AM process, as evident from the stress–strain curve of the Al phase in the HAZ region (cf. Fig. 7 a). In addition, the thermal load during the FSW process causes a change in the composition of the Si-rich phase [12, 33] in the HAZ, which results in a small difference is seen in the tensile behavior of the Si-rich phase, as shown in Fig. 7 e. Changes in the behavior of the Al and Si-rich phases contribute to the strength reduction in HAZ compared to the AM region. However, the strength is much better than WZ and cast regions since the HAZ region retains some characteristics of the AM process. Due to the relative ease of plastic flow caused by the discontinuous Si-rich network [12], the ductility of the HAZ region is better than in the AM region. Similar to the AM RVE, Fig. 7 d and h show an inhomogeneous stress distribution with higher stress distribution in the Si-rich phase.

4.2 Prediction of the hybrid joint tensile properties

Uniaxial tensile simulation is performed on the joint macromodel, shown in Fig. 5, with a J2-plasticity model using ABAQUS [20]. Young's modulus and Poisson's ratio are set as 65,000 MPa and 0.3, respectively. For describing the plastic behavior of the joint regions, the plastic strain and the corresponding stress values are extracted from the stress–strain curve of each joint area obtained from the

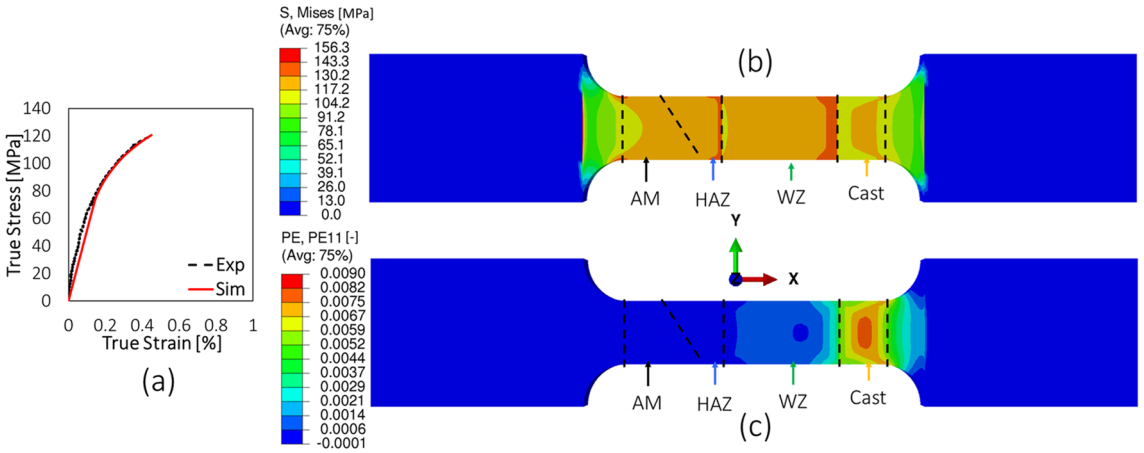

Fig. 8 Tensile behavior of the joint macro model of the hybrid FSW joint. **a** Comparison of stress–strain curve from simulation with the experiment. The experimental results are recompiled from previous study of authors [1]. **b** Von Mises equivalent stress distribution, and **c** plastic strain distribution along the loading direction (*x*-direction)

micromechanical modeling approach (cf. Fig. 6). These stress and plastic strain values are provided as input to ABAQUS [20].

Figure 8 a compares the stress–strain curve from the joint macro model with the experimental result. The experimental results used here are taken from the previous study of some of the authors of present study [1]. The predicted global tensile stress–strain curve of the hybrid FSW joint agrees well with the experimental curve, with a minor variation in the elastic region. Therefore, this method can predict the tensile behavior of the AM-cast FSW joint with reasonable accuracy.

The von Mises equivalent stress distribution of the FSW joint model shows a varying stress distribution along the gauge length (cf. Fig. 8b). Due to the high gradient in the material properties, higher stress accumulates in the WZ-cast and WZ-HAZ interfaces. However, the maximum stress occurring in the middle of the cast region is almost 130 MPa. This is more than the ultimate tensile strength of the cast specimen obtained from the micromechanical model. Similarly, higher plastic strain accumulation occurs in the middle of the cast region and near the radius along the thickness of the specimen (cf. Fig. 8c). This aligns with the DIC measurement reported in the author's previous study [1]. The maximum total strain along the loading direction in these regions is 1.08%, whereas the maximum strain measured using DIC is 0.89% [1]. These regions of high strain and stress accumulation in the cast region act as crack initiation sites of the AM-cast FSW joint. The plastic strain in the weld zone is high at the WZ-cast interface and remains relatively constant until the WZ-HAZ interface, where the WZ remain elastic. Since the applied strain is low, the AM and HAZ regions do not undergo any plastic deformation. Similar to experimental observation in [1], no necking is observed until the maximum elongation of the material, indicating a brittle fracture.

The observations from micromechanical modeling and the joint macromodel indicate that the applied modeling approach can be used to predict the local and global tensile behavior and help to understand the effect of microstructural features on the tensile property of the joint. This understanding can be used to tailor the heat-treatment process in order to improve the mechanical properties of the AM-cast hybrid FSW joint.

5 Conclusion

In the present study, the tensile behavior of a hybrid welded joint of AlSi10Mg parts produced by additive manufacturing (AM) and casting and joined using friction-stir welding (FSW) is predicted at local and global scale. A representative volume element (RVE) is created for each joint region by considering its microstructural features. A hybrid model containing a crystal plasticity (CP) model for the Al phase and J2-plasticity model for Si-rich phase is used to predict the local tensile behavior of each region. The estimated local stress–strain curve of each region is applied to the joint macro model to predict the global tensile properties of the AM-cast hybrid FSW joint. The main conclusions are as follows:

1. The applied hybrid CP-J2 modeling approach accurately predicts the local stress–strain curves of each region. The overall global tensile behavior of the AM-cast FSW joint estimated using the predicted local curves of each region agrees well with the experimental results.

2. The cast and AM regions are the weakest and strongest members of the hybrid FSW joint, respectively. The large grain size and the elongated Si particles obtained as a result of the slow solidification rate during casting are the reasons for the lower strength and ductility of the cast material.
3. The Orowan looping mechanism introduced by fine Si precipitates as well as solid solution strengthening obtained during AM process are reduced in their effect due to severe plastic deformation in the weld zone (WZ) and thermal load in the heat-affect zone (HAZ). This reduces the strength of the Al phase, which, together with the morphology change of the Si-rich phase, reduces the overall strength of the WZ and HAZ regions compared to the AM region.
4. The stress distribution in the cast RVE shows a homogeneous distribution in the Al phase and a much higher stress accumulation at the edge of the Si particles, which could act as potential crack initiation sites. In contrast, an inhomogeneous distribution is observed in AM, HAZ, and WZ RVEs due to the Si-rich phase and the orientations of the Al grains.
5. The joint macro model illustrates a heterogenous stress and strain distribution along the length of the weld joint. The stress accumulation is higher in the WZ-cast and WZ-HAZ interfaces due to the high difference in the material behavior between these regions. A high strain accumulation is observed in the middle of the cast region and at the radius of the specimen. At these regions, the stress reaches the ultimate strength of the cast specimen. These are the sensitive areas for tensile failure, and this observation aligns with the experimental results.

Author contribution All authors contributed to the study conceptualization and methodology. Formal analysis, investigations, visualization, and validation were performed by Aravindh Nammalvar Raja Rajan, Marcel Krochmal, and Thomas Wegener. The FORTRAN and Python codes used in the study were developed by Alexander Hartmaier and Aravindh Nammalvar Raja Rajan. The initial draft of the manuscript was written by Aravindh Nammalvar Raja Rajan, and all authors reviewed and edited the manuscript. Ghazal Moeini and Thomas Niendorf acquired the funding for the study. The present study was performed under the supervision of Alexander Hartmaier, Thomas Niendorf, and Ghazal Moeini. All authors read and approved the final manuscript.

Funding Open Access funding enabled and organized by Projekt DEAL. This research is supported by the German Research Foundation (DFG) (project number: 450156756).

Data availability The data presented in this study are available upon resaonable request from the corresponding author.

Declarations

Conflict of interest The authors declare no competing interests.

References

1. Krochmal M, Nammalvar Raja Rajan A, Moeini G, Sajadifar SV, Wegener T, Niendorf T (2022) Microstructural and mechanical properties of AlSi10Mg: hybrid welding of additively manufactured and cast parts. J Mater Res 38(2):297–311. https://doi.org/10.1557/s43578-022-00838-1
2. Campanelli SL, Casalino G, Contuzzi N, Angelastro A, Antonio Domenico L (2011) Preliminary investigation on hybrid welding of selective laser molten parts, in: International Congress on Applications of Lasers & Electro-Optics, Orlando, FL, USA,: 652–660. https://doi.org/10.2351/1.5062306
3. Emmelmann C, Dipl.-I, Beckmann F (2015) Hybrid lightweight design by laser additive manufacturing and laser welding processes, in: Lasers in Manufacturing Conference
4. Nahmany M, Rosenthal I, Benishti I, Frage N, Stern A (2015) Electron beam welding of AlSi10Mg workpieces produced by selected laser melting additive manufacturing technology. Addit Manuf 8:63–70. https://doi.org/10.1016/j.addma.2015.08.002
5. El Hassanin A, Velotti C, Scherillo F, Astarita A, Squillace A, Carrino L (2017) Study of the solid state joining of additive manufactured components, in: Proceedings of the 3rd International Forum on Research and Technologies for Society and Industry - Innovation to Shape the Future for Society and Industry (RTSI), IEEE. https://doi.org/10.1109/RTSI.2017.8065967
6. Prashanth KG, Damodaram R, Scudino S, Wang Z, Prasad Rao K, Eckert J (2014) Friction welding of Al-12Si parts produced by selective laser melting. Mater Des 57:632–637. https://doi.org/10.1016/j.matdes.2014.01.026
7. Moeini G, Sajadifar SV, Wegener T, Rössler C, Gerber A, Böhm S, Niendorf T (2021) On the influence of build orientation on properties of friction stir welded Al-Si10Mg parts produced by selective laser melting. J Market Res 12:1446–1460. https://doi.org/10.1016/j.jmrt.2021.03.101
8. Moeini G, Sajadifar SV, Wegener T, Brenne F, Niendorf T, Böhm S (2019) On the low-cycle fatigue behavior of friction stir welded Al–Si12 parts produced by selective laser melting. Mater Sci Eng, A 764:138189. https://doi.org/10.1016/J.MSEA.2019.138189
9. Moeini G, Sajadifar SV, Engler T, Heider B, Niendorf T, Oechsner M, Böhm S (2020) Effect of friction stir processing on microstructural, mechanical, and corrosion properties of Al-Si12 additive manufactured components. Metals (Basel) 10:1. https://doi.org/10.3390/met10010085
10. Kim DK, Hwang JH, Kim EY, Heo YU, Woo W, Choi SH (2017) Evaluation of the stress-strain relationship of constituent phases in AlSi10Mg alloy produced by selective laser melting using crystal

plasticity FEM. J Alloys Compd 714:687–697. https://doi.org/10.1016/j.jallcom.2017.04.264
11 Jain R, Yadava M, Nayan N, Gurao NP (2022) Combinatorial synchrotron diffraction-constitutive modelling-crystal plasticity simulation framework for direct metal laser sintered AlSi10Mg alloy. Mater (Oxf) 22:101395. https://doi.org/10.1016/j.mtla.2022.101395
12. Nammalvar Raja Rajan A, Krochmal M, Wegener T, Biswas A, Hartmaier A, Niendorf T, Moeini G (2022) Micromechanical modeling of AlSi10Mg processed by laser-based additive manufacturing: from as-built to heat-treated microstructures. Materials 15(16):5562. https://doi.org/10.3390/ma15165562
13. Nammalvar Raja Rajan A, Krochmal M, Shahmardani M, Wegener T, Hartmaier A, Niendorf T, Moeini G (2023) Micromechanical modeling of the low-cycle fatigue behavior of additively manufactured AlSi10Mg. Mater Sci Eng A 879:145232. https://doi.org/10.1016/j.msea.2023.145232
14. Toursangsaraki M, Li Q, Hu Y, Wang H, Zhao D, Zhao Y (2021) Crystal plasticity modeling for mechanical property prediction of AA2195-T6 friction stir welded joints. Mater Sci Eng A 823:141677. https://doi.org/10.1016/j.msea.2021.141677
15. Gerber A (2020) Schweißbarkeit von AlSi10Mg additiv und konventionell gefertigten Bauteilen mittels Rührreibschweißen, Master thesis, University Kassel
16. Chen B, Moon SK, Yao X, Bi G, Shen J, Umeda J, Kondoh K (2017) Strength and strain hardening of a selective laser melted AlSi10Mg alloy. Scr Mater 141:45–49. https://doi.org/10.1016/j.scriptamat.2017.07.025
17. Roters F, Eisenlohr P, Hantcherli L, Tjahjanto DD, Bieler TR, Raabe D (2010) Overview of constitutive laws, kinematics, homogenization and multiscale methods in crystal plasticity finite-element modeling: theory, experiments, applications. Acta Mater 58:1152–1211. https://doi.org/10.1016/j.actamat.2009.10.058
18. Ma A, Hartmaier A (2014) On the influence of isotropic and kinematic hardening caused by strain gradients on the deformation behaviour of polycrystals. Phil Mag 94:125–140. https://doi.org/10.1080/14786435.2013.847290
19. Boeff M (2016) Micromechanical modelling of fatigue crack initiation and growth, Ph.D. Dissertation, Ruhr Universität Bochum, Universitätsbibliothek
20. Abaqus, Software for finite element analysis, version 2021 (2021) Dassault Systèmes, Vélizy-Villacoublay, France
21. Mises RV (1913) Mechanik der festen Körper im plastisch-deformablen Zustand. Nachr von Der Ges Der Wissenschaften Zu Göttingen, Math-Phy Klasse 1913:582–592
22. Bower A (2009) Applied Mechanics of Solids (1st ed.), CRC Press, Boca Raton, Florida, USA. https://doi.org/10.1201/9781439802489
23. Branch MA, Coleman TF, Li Y (1999) Subspace, interior, and conjugate gradient method for large-scale bound-constrained minimization problems. SIAM J Sci Comput 21:1–23. https://doi.org/10.1137/S1064827595289108
24 Virtanen P, Gommers R, Oliphant TE, Haberland M, Reddy T, Cournapeau D, Burovski E et al (2020) SciPy 1.0: fundamental algorithms for scientific computing in Python. Nat Methods 17:261–272. https://doi.org/10.1038/s41592-019-0686-2
25. Kouznetsova VG (2002) Computational homogenization for the multi-scale analysis of multi-phase materials, Ph.D. Dissertation, Technische Universiteit Eindhoven
26. Biswas A, Prasad MRG, Vajragupta N, Hartmaier A (2020) Kanapy: synthetic polycrystalline microstructure generator with geometry and texture. Zenodo. https://doi.org/10.5281/ZENODO.3662366
27. Bachmann F, Hielscher R, Schaeben H (2011) Grain detection from 2d and 3d EBSD data—specification of the MTEX algorithm. Ultramicroscopy 111:1720–1733. https://doi.org/10.1016/j.ultramic.2011.08.002
28. Biswas A, Prasad MRG, Vajragupta N, ul Hassan H, Brenne F, Niendorf T, Hartmaier A (2019) Influence of microstructural features on the strain hardening behavior of additively manufactured metallic components. Adv Eng Mater 21:7. https://doi.org/10.1002/adem.201900275
29 Groeber MA, Jackson MA (2014) DREAM. 3D: a digital representation environment for the analysis of microstructure in 3D. Integr Mater Manuf Innov 3:56–72. https://doi.org/10.1186/2193-9772-3-5
30 Tsai YC, Chou CY, Lee SL, Lin CK, Lin JC, Lim SW (2009) Effect of trace La addition on the microstructures and mechanical properties of A356 (Al-7Si-0.35Mg) aluminum alloys. J Alloys Compd 487:157–162. https://doi.org/10.1016/j.jallcom.2009.07.183
31 Shakil SI, Hadadzadeh A, ShalchiAmirkhiz B, Pirgazi H, Mohammadi M, Haghshenas M (2021) Additive manufactured versus cast AlSi10Mg alloy: microstructure and micromechanics. Results Mater 10:100178. https://doi.org/10.1016/j.rinma.2021.100178
32. Seifeddine S, Sjögren T, Svensson IL (2007) Variations in microstructure and mechanical properties of cast aluminium ENAC 43100 alloy, Metallurgical Sci Technol. 25
33. Van Cauwenbergh P, Samaee V, Thijs L, Nejezchlebová J, Sedlák P, Iveković A, Schryvers D et al (2021) Unravelling the multi-scale structure–property relationship of laser powder bed fusion processed and heat-treated AlSi10Mg. Sci Rep 11:1. https://doi.org/10.1038/s41598-021-85047-2